ACS ES&T Engineering

pubs.acs.org/estengg

Article

Comparative Infrared Microscopy for Measuring Membrane Thermal Conductivity and Validating Theoretical Heat Transport Models

Tanya Liu and Meagan S. Mauter*

Cite This: *ACS EST Engg.* 2023, 3, 874−882

Read Online

ACCESS | Metrics & More | Article Recommendations | Supporting Information

ABSTRACT: Accurately estimating the effective thermal conductivity of membranes is critical to describing process performance in systems with simultaneous heat and mass transport. Unfortunately, existing approaches for modeling the effective thermal conductivity poorly represent real membrane morphologies. Meanwhile, existing measurement techniques are subject to uncertainties from thermal contact resistances, are prone to large systematic errors with low thermal conductivity samples, or require measurement of multiple additional parameters that each introduce additional sources of error. This work introduces the use of comparative infrared microscopy for directly measuring membrane thermal conductivity in highly porous membrane materials. Comparative infrared microscopy negates the need for absolute measurements of heat flow, additional properties such as heat capacity, or any prior assumptions regarding thermal contact resistances, thus overcoming the shortcomings of prior experimental methods. We demonstrate the use of comparative infrared microscopy on three chemically and morphologically distinct membrane distillation membranes. Our results for a specific PVDF membrane are approximately 30% higher than previously reported values measured with a Lees' disc apparatus, likely due to the influence of additional contact resistances in the Lees' disc measurement. Our measurements confirm that membrane morphology plays a significant role in effective membrane thermal conductivity and suggest that morphology can guide the selection of theoretical models for approximating membrane thermal conductivity when direct measurements are not possible. The fibrous stretched PTFE membrane is best represented by the series conduction model, while the phase inversion PP and PVDF membranes are better represented by the Maxwell-Eucken model. We conclude with recommendations for further refining thermal conductivity models of structurally heterogeneous membrane materials.

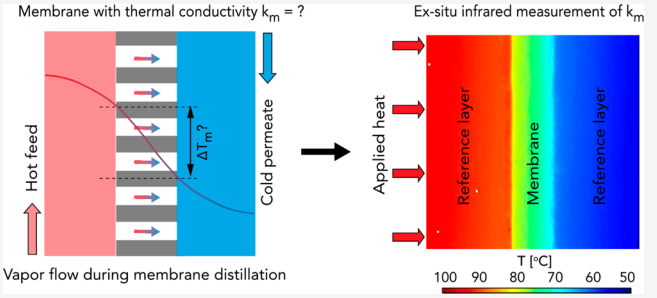

KEYWORDS: *Membrane distillation, thermal conductivity, comparative infrared microscopy, porous materials*

1. INTRODUCTION

The effective thermal conductivity of porous membrane materials is a salient property that governs process performance in a wide range of applications with coupled heat and mass transport. These applications include membrane-based water treatment processes,[1] where porous membranes used to facilitate mass transport simultaneously conduct heat due to internal temperature gradients within the systems. The overall efficiency of these processes is directly related to the amount of heat conducted through the membranes.[2] As a result, accurate estimates of membrane thermal conductivity are critical to predicting final system performance.

One example is membrane distillation (MD), a membrane-based, thermally driven separation technique for desalination and high salinity brine concentration.[3] A key parameter that contributes to uncertainties in MD process optimization is uncertainty in the effective thermal conductivities of the hydrophobic membranes that facilitate phase separation. A schematic of a basic direct-contact MD system is shown in Figure 1, where hot feed flows on one side of the membrane and cold permeate flows on the other. The transmembrane vapor flux is driven by the vapor pressure difference between the hot and cold sides. Parallel parasitic heat conduction through the membrane and gaseous pores, however, can decrease the available driving force for evaporation and lower the overall thermal efficiency of the process, η, where

$$\eta = \frac{Q_l}{Q_l + Q_c} \tag{1}$$

and Q_l and Q_c represent the latent and conductive heat transfer across the membrane, respectively. Previous studies have shown that variation in the membrane thermal conductivity

Received: December 19, 2022
Revised: March 19, 2023
Accepted: March 20, 2023
Published: March 31, 2023

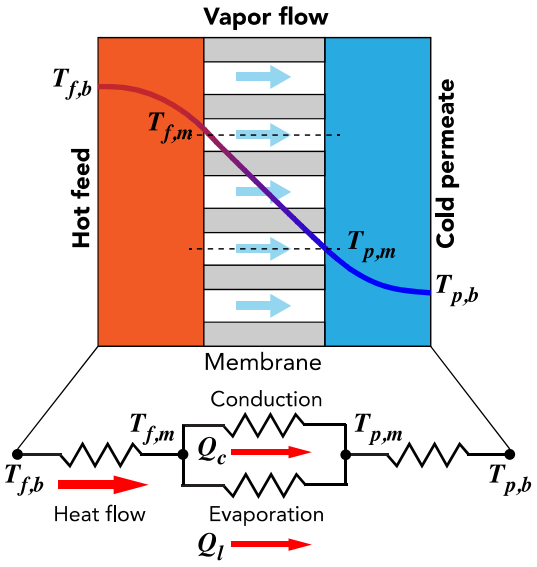

Figure 1. Example of a direct contact membrane distillation process with coupled heat and mass transport. Hot feed flows on one side of a hydrophobic membrane while cold permeate flows on the other. Transmembrane flux is governed by the vapor pressure difference between the two sides, but parasitic heat conduction, Q_c, across the membrane can reduce flux by reducing the amount of latent heat transfer, Q_l. Subscripts f and p refer to feed and permeate properties, respectively, while subscripts b and m distinguish between bulk and membrane surface properties.

from 0.05 to 0.45 $Wm^{-1}K^{-1}$ can reduce the thermal efficiency from 80% to as low as 40%.[4] The levelized cost of water produced with MD has also been found to vary as much as 0.65 $/m^3 of product for each 0.01 $Wm^{-1}K^{-1}$ variation in membrane thermal conductivity.[5]

Past work has employed both modeling and direct measurement approaches for estimating membrane thermal conductivity. Modeling approaches are convenient and eliminate the need for dedicated thermal conductivity measurement setups but typically require simplifying assumptions regarding membrane morphology and structure. These assumptions may not always accurately capture the nature of heat flow through MD membranes, which can have significant structural deviation within a single membrane or between different membrane types depending on the fabrication method.[6,7] The most commonly used model to estimate membrane thermal conductivity is the parallel, or isostrain, conduction model that assumes the gaseous and solid components of the membrane are perfectly aligned parallel to the direction of heat flow.[8,9] While the simplicity of this model enables facile application to a wide range of membranes, the idealized structural assumptions are poor representations of actual membrane morphologies. Previous comparisons of membrane thermal conductivities predicted using simplified conduction models have been shown to deviate from experimentally measured values by as much as 109%.[10]

Validating and improving these conduction models have been constrained by the absence of, and issues with, experimental measurements of membrane thermal conductivity. Membranes are definitionally thin (~100 μm for MD membranes), are easily susceptible to deformation through compression, and often have low effective thermal conductivities (<0.1 $Wm^{-1}K^{-1}$ in the case of MD). The thinness and compressibility of many membranes preclude measurement with traditional steady-state techniques such as the guarded hot plate or Lees' disc methods. These methods typically require sample thicknesses >25 mm[11] and use sample compression to account for the effect of thermal contact resistances.[12] Transient measurement techniques can deconvolute thermal contact resistances without sample compression, but these methods present other barriers that complicate accurate thermal conductivity measurements. The transient plane source method, for instance, is prone to large systematic errors with low thermal conductivity samples, making it potentially unsuitable for many membrane thermal conductivity measurements without the use of custom sensors.[13] The laser flash method only captures thermal diffusivity and requires separate measurements of heat capacity to obtain thermal conductivity, which can introduce additional sources of error. Additionally, the method becomes less accurate with porous samples, as the laser radiation can pass through the sample as opposed to creating an idealized surface heat flux.[14] Some studies have also attempted to use MD itself as an indirect thermal conductivity measurement technique,[15] but this approach relies on a wide range of assumptions regarding other heat and mass transfer parameters in the MD process that are historically poorly characterized.[16−18]

Past efforts to reconcile membrane thermal conductivity models[1,9,10] with experimental validation have relied upon a single experimental data set generated through a modified Lees' disc method.[19,20] In lieu of compression, the authors measured the total thermal resistance across stacks of multiple membranes to extract the thermal contact resistances at interfaces between the heating/cooling discs and membranes.[20] Though these results were a valuable contribution for initial validation of different membrane thermal conductivity models, they did not explicitly account for contact resistances at membrane−membrane interfaces, which is likely to underestimate the true effective membrane thermal conductivity.

This paper proposes the use of comparative infrared (IR) microscopy for directly measuring the thermal conductivity of membranes with diverse chemistries and morphologies. In contrast with the previously mentioned experimental approaches, this technique is not impacted by thermal contact resistances and is well-suited to measuring low thermal conductivity samples (<0.1 $Wm^{-1}K^{-1}$) in the range of expected values for MD membranes. The technique has been successfully applied to a wide range of other difficult to measure sample types including nanoscale semiconductor thin films,[21] nanostructured composites,[22] and highly porous aerogels.[23]

The present work describes the general theory behind comparative IR microscopy and articulates a measurement and experimental design approach that accommodates a diverse set of membrane chemistries and morphologies. We then demonstrate successful application of the methodology to measure the thermal conductivity of three different commercial MD membranes. We compare our results against previously reported experimental values obtained through a modified Lees' disc method[19,20] as well as various conduction model predictions to demonstrate the impact of membrane morphology on thermal conductivity. Finally, we offer recommendations for future work to further refine thermal conductivity models of membranes with diverse structural morphologies.

https://doi.org/10.1021/acsestengg.2c00436
ACS EST Engg. 2023, 3, 874−882

2. COMPARATIVE INFRARED MICROSCOPY

2.1. Operating Principles and Theory. In contrast with absolute measurement techniques, comparative thermal conductivity measurement methods do not require direct measurement of heat flux. The sample of interest, in this case a membrane, is instead placed in series with reference layers of known thermal conductivity. After application of a one-dimensional heat flux, the effective thermal conductivity of the membrane can be extracted by comparing the temperature gradient across the reference layers to the temperature gradient across the membrane as

$$k_m = k_r \frac{dT_r}{dx} / \frac{dT_m}{dx} \quad (2)$$

where the subscripts m and r refer to membrane and reference layer properties, respectively.

As seen from eq 2, accurate extraction of membrane thermal conductivity k_m requires accurate measurement of the representative temperature gradients in the membrane and reference layers. Typical contact-based temperature sensors such as thermocouples are poorly suited for this purpose due to their large size (~200 μm) relative to typical membrane thicknesses (~100 μm). Even if such sensors could be integrated nonintrusively, there remains the issue of contact resistances between the sensors and measurement surfaces.

Infrared temperature imaging presents an opportunity for noninvasive measurement of the temperature gradients within the membrane and reference layers. Since IR imaging can resolve a two-dimensional spatial temperature map, the temperature gradients within the layers can be directly measured independent of contact resistances at the layer interfaces. An additional requirement of IR measurements, however, is that the IR emissivities of the measurement surfaces must be known in advance. This requires either a calibration step to extract the emissivities of the membrane/reference layers prior to temperature measurements or surface coating with a high emissivity material such as graphite. In our approach, we use a calibration step that is described further in the Materials and Methods section.

A schematic outlining the basic principles of comparative infrared microscopy is shown in Figure 2. Heat flows from the left to the right in series through a hot side reference layer, a membrane with thickness t_m and width/length L, and a cold side reference layer. The bottom cross-sectional surfaces are assumed to be adiabatic, while the top cross-sectional surfaces are exposed for IR imaging. Since the membranes are easily deformed, cross-sectioning procedures may create a smeared layer of thickness t_s with properties that deviate from the membrane bulk. The error in measured surface temperature gradient attributed to this smeared layer can be minimized by choosing a sufficiently large membrane sample area such that conductive heat transfer through the bulk still dominates, as will be discussed in the next section.

2.2. Sources of Uncertainty. The accuracy of this comparative measurement method relies on two primary assumptions. First, the heat flux going through the membrane and reference layers should be the same. Second, the temperature gradients in the membrane/reference layers measured at the IR imaging surfaces should be representative of the temperature gradients in the bulk. Heat loss from the membrane/reference layer stack can challenge both assumptions, while distortion of the membrane IR imaging surface during sample preparation can impact the latter.

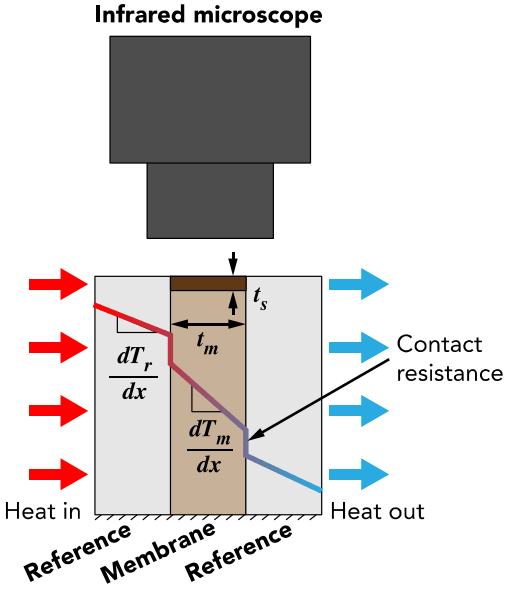

Figure 2. Basic principles of comparative infrared microscopy. A membrane sample of interest with thickness t_m (~100 μm) is placed in series between two reference layers with known thermal conductivities (figure not to scale). The effective thermal conductivity of the membrane is extracted by applying a one-dimensional heat flux and comparing the temperature gradient across the membrane to the temperature gradients in the reference layers. Temperature drops due to contact resistances at membrane/reference interfaces are visualized in the schematic but do not affect the extracted temperature gradients. Cross-sectioning of the membrane during sample preparation can create a distorted layer (thickness t_s) near the IR imaging surface with properties that deviate from bulk values, though this effect can be minimized by choosing a sufficiently large membrane sample area such that heat flux through the sample is dominated by transport through an unperturbed membrane.

Convective/radiative heat loss from the sample stack is particularly problematic for low k samples, where the resistance to thermal conduction through the stack can be comparable to the convective/radiative resistances to the ambient environment. This can result in dissimilar conductive heat fluxes through the membrane and reference layers, which becomes apparent experimentally if the measured hot side reference layer temperature gradient is significantly larger than the cold side reference layer gradient. Heat loss from the IR imaging surfaces can also result in measured temperature gradients that are lower than temperature gradients in the bulk, typically leading to an overestimation of the effective membrane thermal conductivity.

We address the issue of heat loss during our experiments by minimizing the ratio of the membrane thermal conduction resistance relative to the ambient convection/radiation resistances. We designed the experimental apparatus to accommodate membrane samples with large cross-sectional areas for conduction (28 × 28 mm) relative to the exposed IR imaging area for convective/radiative heat loss (~0.1 × 28 mm). Based on calculations with a typical natural convection heat transfer coefficient (~10 $Wm^{-2}K^{-1}$) and a linearized radiation heat transfer coefficient, we estimate a conduction to convection/radiation resistance ratio of approximately 1:7,500 for a typical membrane sample with k_m ~ 0.05 $Wm^{-1}K^{-1}$

https://doi.org/10.1021/acsestengg.2c00436
ACS EST Engg. 2023, 3, 874−882

(further details available in Section S1). This ensures that the majority of the applied heat flux passes through the sample stack via conductive heat transfer and that there is negligible convective/radiative heat loss.

A large conduction cross-sectional area also helps to mitigate the effect of membrane distortion near the imaging surface. Due to the pliant and highly porous nature of the membranes, cross-sectioning with a razor blade or other similar methods can result in smearing or pore closure up to a certain depth t_s below the cross-sectioned surface. The reduction in porosity of this layer results in a higher effective thermal conductivity than the bulk membrane and can lead to overestimation of the effective membrane thermal conductivity. We performed finite element simulations for a worst-case scenario where an entire top layer of the membrane with thickness t_s is solid with no pore openings remaining. Results from our simulations showed that, even with severe distortion over a thick layer of t_s = 10 μm, the extracted membrane thermal conductivity overpredicts the bulk effective thermal conductivity by less than 10% (further details available in Section S2). This is due to the large remaining cross-sectional area for conductive heat transfer through the bulk, which helps to ground the measured temperature gradient even if there is significant deviation of the membrane morphology near the imaging surface.

Finally, we note that the comparative IR measurement method employed here characterizes the effective thermal conductivity of the membranes ex situ with ambient air as opposed to water vapor as the gaseous component. Since parasitic conduction heat transfer across the membrane in aqueous separation processes such as MD involves conduction through both the solid matrix and gaseous pores, this ex situ approach is not a perfect representation of conduction in MD systems. Due to the relatively minimal difference in thermal conductivity between water vapor and air (0.016 $Wm^{-1}K^{-1}$ versus 0.026 $Wm^{-1}K^{-1}$), however, we believe any insight gained into conduction model selection based on experimental results will still be directly translatable to MD systems in which membranes are not significantly wetted out.

3. MATERIALS AND METHODS

An overview of the experimental setup is provided in Figure 3. The membrane is placed between two polycarbonate (PC) sheets approximately 0.79 mm thick that act as reference layers. The thermal conductivity of the PC layers was characterized to be 0.21 ± 0.02 $Wm^{-1}K^{-1}$ in separate laser flash measurements prior to the IR experiments. Heating and cooling across the PC/membrane stack is sustained by copper blocks linked to a ceramic heater and chiller, respectively. The copper blocks provide thermal mass to stabilize the heat flow throughout the system and house embedded thermocouples that provide reference temperature measurements during emissivity calibration. The top surfaces of the copper blocks and PC/membrane stack are exposed to ambient to provide a viewing window for IR measurements, and the remaining surfaces are insulated with approximately 1 cm thick of Delrin plastic. The heater/hot side copper block assembly is mounted on a linear shaft and integrated with an in-line load cell to ensure consistent compression (~20 kPa) of the membranes during measurements. This applied pressure is comparable to typical pressure differences across an MD membrane with feed/permeate temperatures of approximately 65 °C/25 °C, respectively.

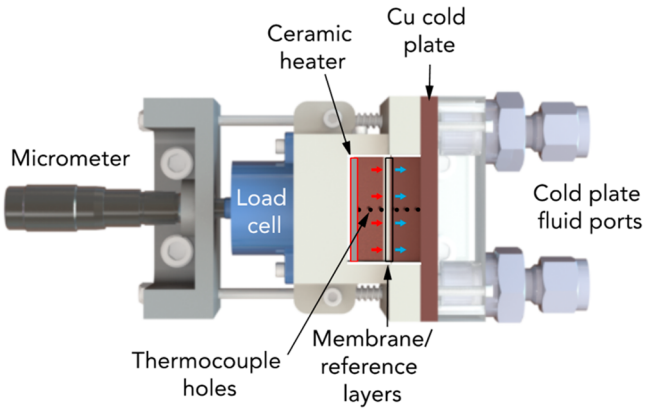

Figure 3. Schematic of experimental setup. Heating and cooling across the PC/membrane stack is sustained by copper blocks linked to a ceramic heater and chiller, respectively. The hot side copper block assembly is mounted on a linear shaft and integrated with an in-line load cell to ensure consistent compression of the membranes during measurements.

An IR microscope (QFI Infrascope) is used in lieu of a standard IR camera to provide the necessary spatial resolution (2.7 μm per pixel) to extract the temperature gradient across the relatively thin membrane samples (~100 μm). Prior to temperature data collection, a calibration procedure is performed to generate a pixel-by-pixel emissivity map for the membrane/polycarbonate surfaces. During the calibration procedure, the membrane/PC stack is first heated to a uniform temperature of 70 °C. This temperature represents the average membrane temperature during the IR thermal conductivity measurements and is chosen to maximize the IR signal while still maintaining a temperature representative of MD conditions. Once the hot side and cold side embedded thermocouples show a fluctuation of less than 0.1 °C over a 3 min period, the steady-state temperature criterion is established. The IR microscope software then uses the radiance readings at the known temperature of 70 °C to create a spatial map of emissivity over the imaging window.

After emissivity calibration, the generated emissivity map is stored to translate future radiance readings under powered conditions with applied heat fluxes to absolute temperature readings. During thermal conductivity measurements, a one-dimensional temperature gradient is established by reducing the chiller temperature to 30 °C and applying approximately 9W of power from the ceramic heater. Once a steady-state temperature distribution is established across the stack, a two-dimensional IR temperature map is captured using a 15× magnification lens over a 790 × 790 μm imaging window. Measurements are performed at approximately 3 different imaging windows per sample.

Table 1 summarizes the properties of the commercial membranes investigated in this study. Three different

Table 1. Properties of Commercial PTFE, PP, and PVDF Membranes Considered in This Study

manufacturer	membrane type	porosity [%]	thickness [μm]	pore diameter [μm]
Sartorious	PTFE	62	60	0.2
3M	PP	84	160	0.2
Millipore	PVDF	62	109	0.2

https://doi.org/10.1021/acsestengg.2c00436
ACS EST Engg. 2023, 3, 874−882

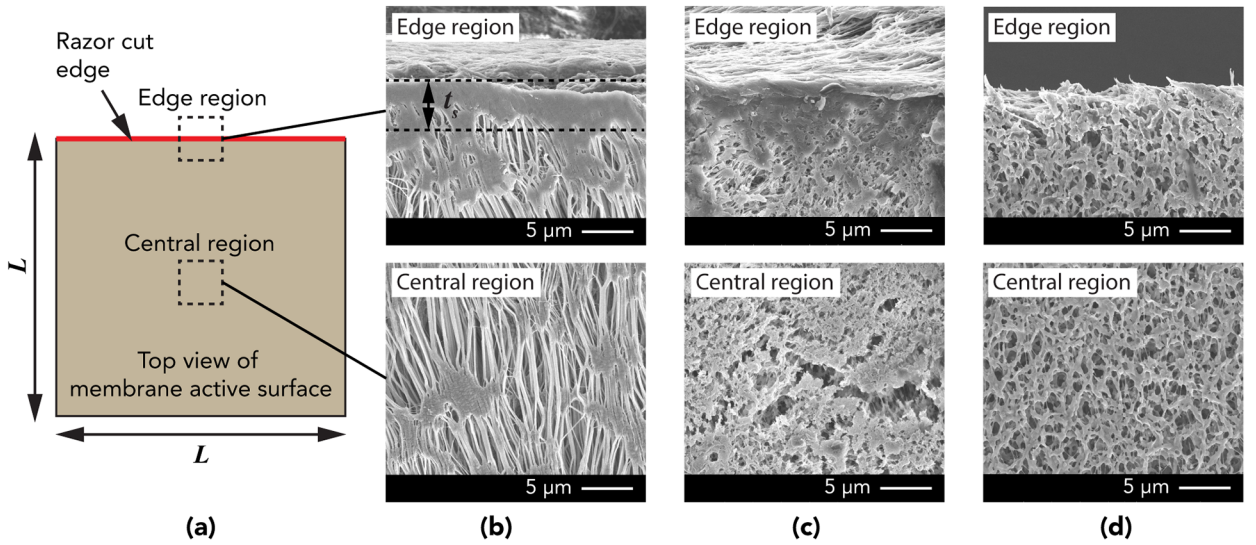

Figure 4. SEM analysis to determine the extent of membrane distortion after razor cross-sectioning. (a) Schematic showing approximate locations of top view SEM images of the membrane active surface (width/length L) relative to the razor cut IR imaging edge (cross-sectioned surface shown going into the page). Comparison of SEMs of the bulk membrane regions in the center of the active area versus near the razor cut edges shows relatively minimal distortion of the membrane below the cross-sectioned surface with thickness of the smeared layer t_s ranging from ~2 to 4 μm for the (b) PTFE, (c) PP, and (d) PVDF membranes.

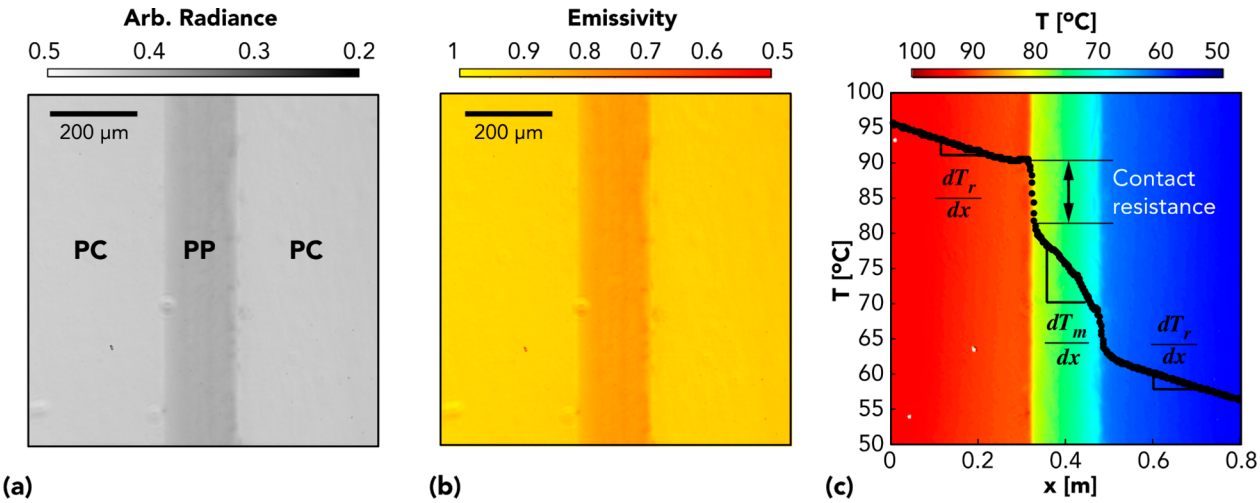

Figure 5. Representative sequence of typical IR images during data collection. (a) Unpowered radiance image at 70 °C during emissivity calibration for a PP membrane with arbitrary radiance units. (b) Generated emissivity map after calibration. PC layers have emissivity of 0.92 ± 0.02 while typical PP membrane emissivity values were 0.82 ± 0.02. (c) Spatial temperature map with applied one-dimensional heat flux overlaid with area averaged temperature gradients used to extract k_m. Temperature drops at PC/PP interfaces are attributed to thermal contact resistances.

membranes were chosen to provide a representative set of membranes made from different materials (PTFE, PP, and PVDF), membranes with similar porosity but different morphology (fibrous PTFE versus phase inversion PVDF), and membranes with similar morphology but varying porosity (PP versus PVDF). Porosities, thicknesses, and pore diameters are given based on manufacturer provided values and previous measurements reported elsewhere.[24]

Each membrane is cross-sectioned with a razor blade to provide an exposed surface for IR imaging. Top view SEMs of the central membrane bulk region were compared against the razor cut edge region (Figure 4a) for the PTFE (b), PP (c), and PVDF (d) membranes. As seen in the panels, all three membranes show minimal distortion relative to the bulk morphology near the razor cut edge. Even though some pore closure is observed for the PTFE and PP membranes after razor cutting, the distorted region remains small with $t_s \sim 2-4$ μm. We therefore determined razor cutting to be an acceptable cross-sectioning method for the IR measurements with relatively minimal influence on the extracted k_m.

4. THERMAL CONDUCTIVITY MEASUREMENT RESULTS

An example of a typical IR imaging sequence is shown for a PP membrane in Figure 5: (a) an unpowered radiance image during emissivity calibration at 70 °C and (b) the generated emissivity map. Typical emissivity values for the PC reference layers in our study are 0.92 ± 0.02 across all reported measurements, while typical emissivity values for the PTFE, PP, and PVDF membranes are 0.79 ± 0.03, 0.82 ± 0.02, 0.72 ± 0.03, respectively. Figure 5c shows the steady-state spatial

https://doi.org/10.1021/acsestengg.2c00436
ACS EST Engg. 2023, 3, 874−882

temperature map after an applied one-dimensional heat flux, overlaid with the area averaged temperature profile used to extract k_m. The effect of contact resistances is apparent due to the temperature drops visible at the membrane/PC interfaces, emphasizing the advantage of a noncontact IR measurement technique over traditional measurement approaches. The reference PC temperature gradient, dT_r/dx, is taken as the average of the hot and cold side PC gradients. Typical deviation between the hot and cold side PC gradients is less than 5%, confirming minimal heat loss across the stack.

A summary of the measurement results for the effective thermal conductivities of the PTFE, PP, and PVDF membranes is shown in Figure 6. The experimental values for each membrane type represent measurements across 3 different samples with 3 different imaging windows per sample. Average values of k_m for the PTFE, PP, and PVDF membranes are 0.034 ± 0.004, 0.056 ± 0.004, and 0.074 ± 0.012 $Wm^{-1}K^{-1}$, respectively. As seen in the figure, most measurement results fall within ±15% of the average values. Both inter- and intrasample variability are observed, which may be partially attributed to inherent local variations in membrane morphology. Distortion of the membrane during cross-sectioning may also contribute to some intersample variability, though this impact is expected to be small as discussed in the previous section.

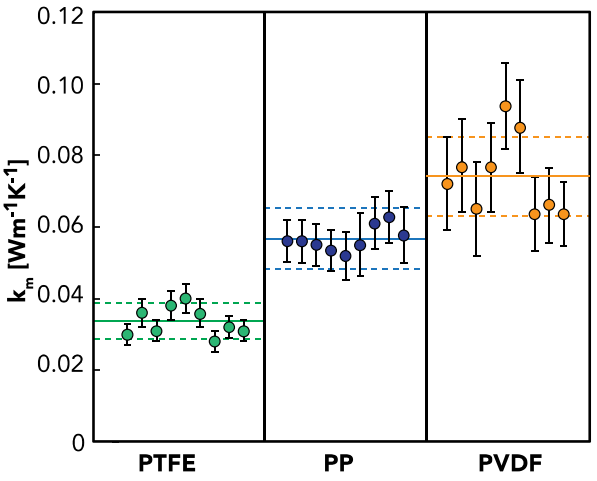

Figure 6. Summary of measurement results for PTFE, PP, and PVDF membranes. Experimental values represent measurements across 3 different samples per membrane type, with 3 imaging windows per sample. Solid line represents average k_m values, while dashed lines represent ±15% from the average.

We note that the experimental values for the PVDF membrane are approximately 30% higher than previously reported values for the same type of membrane characterized as part of a multiple membrane stack with a Lees' disc apparatus.[20] This may be due to the fact that the previous study did not explicitly account for membrane−membrane interfacial resistances, likely resulting in an underprediction of k_m. In the previous method, the authors assumed that the membrane−membrane interfacial resistances would be represented in the y-intercept of experimental data for the total thermal resistance of a membrane stack versus the number of membranes. However, the contribution of membrane−membrane interfacial resistances is also dependent on the number of membranes and cannot be eliminated based on the y-intercept only.

5. DISCUSSION

We compare our measurement results against model predictions based on the parallel, series, and Maxwell-Eucken model formulations to identify models approximating each membrane type. As seen in Figure 7a, the three different models are derived based on different assumptions regarding the distribution of the solid and gaseous components in a porous medium. The parallel or isostrain model assumes that the gaseous or solid components are aligned parallel to the direction of heat flow, while the series or isostress model

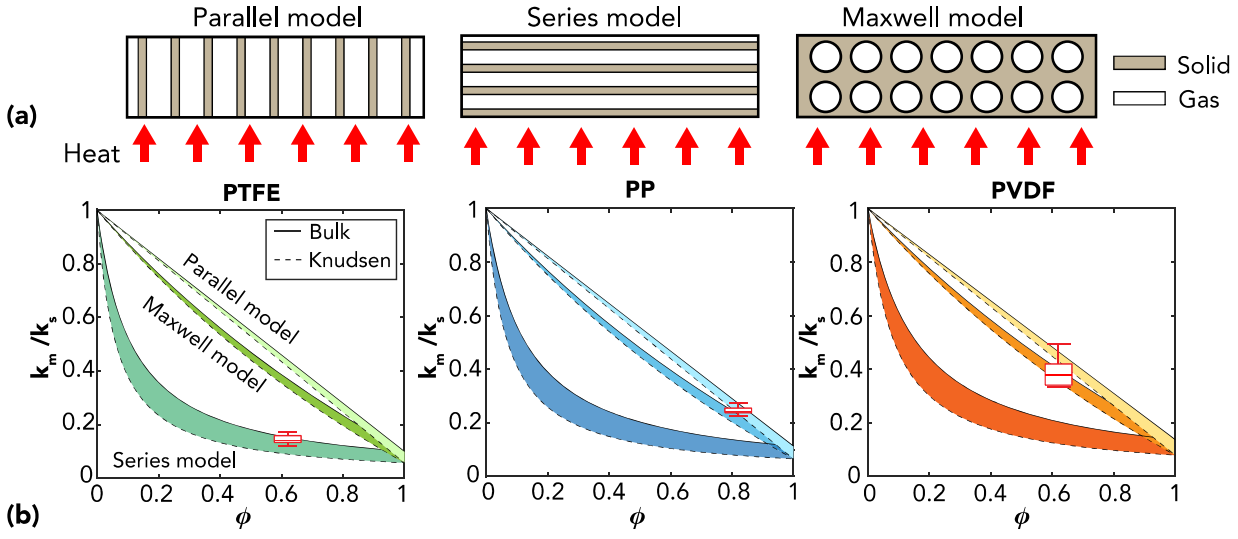

Figure 7. Comparison of measured k_m values against model predictions. (a) Illustrations of parallel, series, and Maxwell models commonly used for conduction in porous media. (b) Comparison of experimental results for PTFE, PP, and PVDF membranes against different model predictions for k_m/k_s as functions of porosity. Dashed and solid lines represent model predictions with/without Knudsen effects limiting air thermal conductivity, respectively. The effective thermal conductivity of the PTFE aligns well with series model predictions, while the effective thermal conductivity of PP and PVDF membranes are well-described by the Maxwell model.

https://doi.org/10.1021/acsestengg.2c00436
ACS EST Engg. 2023, 3, 874−882

assumes alternating layers of gaseous and solid component aligned perpendicular to the direction of heat flow. These models represent the upper and lower bounds to the effective thermal conductivity of a porous medium, respectively, with the following formulations of

$$k_m = \phi k_g + (1 - \phi)k_s \tag{3}$$

for the parallel model and

$$k_m = \left(\frac{\phi}{k_g} + \frac{(1 - \phi)}{k_s}\right)^{-1} \tag{4}$$

for the series model. ϕ is the porosity of the membrane, and k_g and k_s represent the thermal conductivities of the gaseous and solid components, respectively.

The Maxwell-Eucken model assumes that the gaseous component is distributed in the form of spherical inclusions within a continuous solid matrix.[25] The effective thermal conductivity in this case is described as

$$k_m = k_s \frac{2k_s + k_g - 2(k_s - k_g)\phi}{2k_s + k_g + (k_s - k_g)\phi} \tag{5}$$

We model the gaseous component (air) assuming both bulk properties and accounting for the possibility of the Knudsen effect, where the air thermal conductivity is reduced below bulk values due to mean free path confinement in the membrane pores. The mean free path of air can be calculated as

$$l = \frac{k_B T}{\pi\sqrt{2}\,\sigma p} \tag{6}$$

where k_B is the Boltzmann constant, T is the air temperature, σ is the air molecular diameter, and p is the pressure. At 70 °C, the average membrane temperature during thermal conductivity measurements, l, is approximately 76 nm. For the average pore sizes d_p considered in this study (0.2 μm), this corresponds to a Knudsen number l/d_p of 0.38, confirming the possibility of a Knudsen-limited gaseous thermal conductivity.

The reduced gaseous thermal conductivity due to the Knudsen effect can be calculated as

$$k_g' = \frac{k_g}{1 + \beta Kn} \tag{7}$$

where β is a dimensionless parameter that accounts for collisions between the gas molecules and surrounding solid and is approximately equal to 2 for air.[26,27] Assuming Kn = 0.38, this results in a k_g' of approximately 0.015 $Wm^{-1}K^{-1}$ for the parameters considered in this study.

The model predictions for the ratio of k_m/k_s assuming bulk air properties and accounting for the Knudsen effect are plotted as a function of porosity in Figure 7b. The effective thermal conductivities of the solid PTFE, PP, and PVDF polymers are based on averages of reported values in the literature and are taken as 0.26,[28−30] 0.23,[28,31,32] and 0.19 $Wm^{-1}K^{-1}$,[28,29,33,34] respectively. As seen in the panels, the PP and PVDF effective thermal conductivity values are well represented by the Maxwell-Eucken model, while the PTFE effective thermal conductivity values more closely agree with series model predictions.

These findings are potentially due to the differences in membrane morphology between the three membranes. The PTFE membranes considered in this study are fabricated through a biaxial mechanical stretching process that results in layers of PTFE fibers with in-plane alignment. Cross-plane heat flow through these layers of stacked fibers therefore much more closely resembles the series conduction model scenario, where there is minimal cross-plane connectivity between the solid fibers. The relatively low thermal conductivity values observed for the PTFE membrane also suggest that there may be Knudsen effects that limit the gaseous thermal conductivity, though further experiments under varying levels of vacuum would be necessary to confirm this.

The PP and PVDF membranes, in contrast, are fabricated through phase inversion methods that result in more isotropic distributions of the gaseous and solid components. Since the solid phase is connected and relatively continuous throughout the membranes, heat can still flow preferentially through the solid with relatively minimal influence from the gaseous component. These types of structures are morphologically similar to the porous medium approximation made by the Maxwell-Eucken model, as evidenced by the agreement between model predictions and experimental results (approximately 6% and 4% deviation for the PP and PVDF membranes, respectively).

The potential influence of membrane morphology on effective thermal conductivity is most strongly evidenced when comparing the PTFE membrane against the PVDF membrane results. The two membranes have approximately equivalent porosities and pore sizes. Solid PTFE also has a higher thermal conductivity than solid PVDF. Applying the common parallel model assumption to both membranes would incorrectly predict a higher PTFE thermal conductivity, when in fact the measurement results demonstrate that the PTFE has a much lower thermal conductivity.

The commonly used parallel or isostrain model is not an accurate predictor for the effective thermal conductivity of any of the three membranes. Notably, it overpredicts k_m for the PTFE membrane by more than 200% and overestimates k_m for the PP and PVDF membranes by approximately 11% and 21%, respectively. We note that the greater parallel model error for the PVDF membrane may be due to its lower porosity. As seen in Figure 7b, the Maxwell-Eucken model approaches the parallel model at very high porosities above approximately 0.9. At lower porosities ranging from approximately 30% to 80%, however, the Maxwell-Eucken model shows greater deviation from the parallel model.

As evidenced by the plots, both the parallel and Maxwell-Eucken models are less sensitive to the impact of possible Knudsen-limited gas thermal conductivity. This is because the heat can more preferentially flow through the solid in both model approximations, while heat must pass through the gas and solid in equal amounts in the series model. This suggests that parallel/Maxwell-Eucken-type membranes will be less sensitive to variations in gas properties relative to series model-type membranes.

6. CONCLUSIONS

In this study, we successfully measured the effective thermal conductivity of three different MD membranes (fibrous stretched PTFE, phase inversion PP and PVDF) using a comparative infrared microscopy technique. The method enables direct measurements without the need for any absolute measurements of heat flow, additional properties such as heat capacity, or any prior assumptions regarding thermal contact

https://doi.org/10.1021/acsestengg.2c00436
ACS EST Engg. 2023, 3, 874−882

resistances. The average measured thermal conductivity values for the PTFE, PP, and PVDF membranes are 0.034 ± 0.004, 0.056 ± 0.004, and 0.074 ± 0.012 $Wm^{-1}K^{-1}$, respectively. Our reported PVDF values are approximately 30% higher than previously reported values obtained with a Lees' disc apparatus;[20] we hypothesize that this may be due to the influence of additional contact resistances in the Lees' disc measurement.

Based on a comparison of our experimental results against different conduction model estimates, we demonstrated that membrane morphology may potentially play an important role in determining the effective thermal conductivity. The fibrous stretched PTFE membrane is well-described by the series model, while the phase inversion PP and PVDF membranes are better represented by the Maxwell-Eucken model. While a larger set of data with additional types of membranes is necessary to draw further conclusions on which models should be used for which membranes, we recommend reconsideration of the parallel/isostrain model as the most generally used membrane thermal conductivity model in MD studies. If experimental data is not available, we encourage researchers to select an appropriate conduction model representative of a simplified morphology that most closely aligns with the membrane of interest. The parallel model can provide a reasonable approximation for membrane morphologies with more isotropic pore distributions but can lead to larger errors for membranes that have greater in-plane fiber alignment. Future experiments on a wider range of membranes with the comparative IR method demonstrated here will be able to provide further guidance on model selection.

■ ASSOCIATED CONTENT

Supporting Information

The Supporting Information is available free of charge at https://pubs.acs.org/doi/10.1021/acsestengg.2c00436.

(1) Estimation of heat loss from the membrane surface, (2) finite element simulations on the impact of membrane deformation near the IR imaging surface, and (3) additional IR images of PTFE and PVDF membranes (PDF)

■ AUTHOR INFORMATION

Corresponding Author

Meagan S. Mauter − *Department of Civil and Environmental Engineering, Stanford University, Stanford, California 94305, United States;* orcid.org/0000-0002-4932-890X; Email: mauter@stanford.edu

Author

Tanya Liu − *Department of Civil and Environmental Engineering, Stanford University, Stanford, California 94305, United States*

Complete contact information is available at: https://pubs.acs.org/10.1021/acsestengg.2c00436

Author Contributions

CRediT: **Tanya Liu** conceptualization, data curation, formal analysis, investigation, methodology, validation, visualization, writing-original draft; **Meagan S Mauter** funding acquisition, project administration, resources, supervision, validation, writing-review & editing.

Notes

The authors declare no competing financial interest.

■ ACKNOWLEDGMENTS

This material is based upon work supported by the U.S. Department of Energy, Solar Energy Technologies Office, Award# DE-EE0008397, and the National Alliance for Water Innovation (NAWI), funded by the U.S. Department of Energy, Energy Efficiency and Renewable Energy Office, Advanced Manufacturing Office under Funding Opportunity Announcement DE-FOA-0001905. The authors thank the Stanford Nanoheat group for generous use of their IR microscope.

■ REFERENCES

(1) Ismail, M. S.; Mohamed, A. M.; Poggio, D.; Pourkashanian, M. Direct contact membrane distillation : A sensitivity analysis and an outlook on membrane effective thermal conductivity. *J. Membr. Sci.* **2021**, *624*, 119035.

(2) Burheim, O. S.; Su, H.; Pasupathi, S.; Pharoah, J. G.; Pollet, B. G. Thermal conductivity and temperature profiles of the micro porous layers used for the polymer electrolyte membrane fuel cell. *Int. J. Hydrogen Energy.* **2013**, *38*, 8437−8447.

(3) Deshmukh, A.; Boo, C.; Karanikola, V.; Lin, S.; Straub, A. P.; Tong, T.; Warsinger, M.; Elimelech, M. Membrane distillation at the water-energy nexus: limits, opportunities, and challenges. *Energy Environ. Sci.* **2018**, *11*, 1177−1196.

(4) Al-obaidani, S.; Curcio, E.; Macedonio, F.; Di Profio, G.; Al-hinai, H.; Drioli, E. Potential of membrane distillation in seawater desalination : Thermal efficiency. *sensitivity study and cost estimation* **2008**, *323*, 85−98.

(5) Bartholomew, T. V.; Dudchenko, A. V.; Siefert, N. S.; Mauter, S. Cost optimization of high recovery single stage gap membrane distillation. *J. Membr. Sci.* **2020**, *611*, 118370.

(6) Eykens, L.; De Sitter, K.; Dotremont, C.; Pinoy, L.; Van Der Bruggen, B. Membrane synthesis for membrane distillation : A review. *Sep. Purif. Technol.* **2017**, *182*, 36−51.

(7) Tijing, L. D.; Choi, J.; Lee, S.; Kim, S.; Kyong, H. Recent progress of membrane distillation using electrospun nano fi brous membrane. *J. Membr. Sci.* **2014**, *453*, 435−462.

(8) Gryta, M.; Tomaszewska, M. Heat transport in the membrane distillation process. *J. Membr. Sci.* **1998**, *144*, 211−222.

(9) Eykens, L.; De Sitter, K.; Dotremont, C.; Pinoy, L.; Van Der Bruggen, B. How To Optimize the Membrane Properties for Membrane Distillation : A Review. *Ind. Eng. Chem. Res.* **2016**, *55*, 9333−9343.

(10) Phattaranawik, J.; Jiraratananon, R.; Fane, A. G. Heat transport and membrane distillation coefficients in direct contact membrane distillation. *Journal of Membrane Science* **2003**, *212*, 177−193.

(11) Salmon, D. Thermal conductivity of insulations using guarded hot plates including recent developments and sources of reference materials. *Meas. Sci. Technol.* **2001**, *12*, R89.

(12) Radhakrishnan, A.; Lu, Z.; Kandlikar, S. G. Effective Thermal Conductivity of Gas Diffusion Layers Used in PEMFC : Measured with Guarded-Hot-Plate Method and Predicted by a Fractal Model. *ECS Trans.* **2010**, *33*, 1163−1176.

(13) Zheng, Q.; Kaur, S.; Dames, C.; Prasher, R. S. Analysis and improvement of the hot disk transient plane source method for low thermal conductivity materials. *Int. J. Heat Mass Transfer* **2020**, *151*, 119331.

(14) García, E.; Osendi, M. I.; Miranzo, P. Thermal diffusivity of porous cordierite ceramic burners. *J. Appl. Phys.* **2002**, *92*, 2346−2349.

(15) Vanneste, J.; Bush, J. A.; Hickenbottom, K. L.; Marks, C. A.; Jassby, D.; Turchi, C. S.; Cath, T. Y. Novel thermal e ffi ciency-based model for determination of thermal conductivity of membrane distillation membranes. *J. Membr. Sci.* **2018**, *548*, 298−308.

(16) Dudchenko, A. V.; Hardikar, M.; Xin, R.; Joshi, S.; Wang, R.; Sharma, N.; Mauter, M. S. Impact of module design on heat transfer in membrane distillation. *J. Membr. Sci.* **2020**, *601*, 117898.
(17) Dudchenko, A. V.; Mauter, M. S. Neural networks for estimating physical parameters in membrane distillation. *J. Membr. Sci.* **2020**, *610*, 118285.
(18) Dudchenko, A. V.; Hardikar, M.; Anand, A.; Xin, R.; Wang, R.; Gopu, C.; Mauter, M. S. Guidance on Nusselt Number Correlation Selection in Membrane Distillation. *ACS ES&T Eng.* **2022**, *2*, 1425.
(19) Izquierdo-gil, M. A.; Garcia-Payo, M. C.; Fernandez-Pineda, C. Air gap membrane distillation of sucrose aqueous solutions. *J. Membr. Sci.* **1999**, *155*, 291−307.
(20) Garcia-Payo, M. C.; Izquierdo-Gil, M. A. Thermal resistance technique for measuring the thermal conductivity of thin microporous membranes. *J. Phys. D. Appl. Phys.* **2004**, *37*, 3008−3016.
(21) Dunham, M. T.; Barako, M. T.; Cornett, J. E.; Gao, Y.; Haidar, S.; Sun, N.; Asheghi, M.; Chen, B.; Goodson, K. E. Experimental Characterization of Microfabricated Thermoelectric Energy Harvesters for Smart Sensor and Wearable Applications. *Adv. Mater. Technol.* **2018**, *3*, 1700383.
(22) Marconnet, A. M.; Yamamoto, N.; Panzer, M. A.; Wardle, B. L.; Goodson, K. E. Thermal conduction in aligned carbon nanotube-polymer nanocomposites with high packing density. *ACS Nano* **2011**, *5*, 4818−4825.
(23) Fan, Z.; Marconnet, A.; Nguyen, S. T.; Lim, C. Y. H.; Duong, H. M. Effects of heat treatment on the thermal properties of highly nanoporous graphene aerogels using the infrared microscopy technique. *Int. J. Heat Mass Transfer* **2014**, *76*, 122−127.
(24) Leitch, M. E.; Lowry, G. V.; Mauter, M. S. Characterizing convective heat transfer coe ffi cients in membrane distillation cassettes. *J. Membr. Sci.* **2017**, *538*, 108−121.
(25) Carson, J. K.; Lovatt, S. J.; Tanner, D. J.; Cleland, A. C. Thermal conductivity bounds for isotropic, porous materials. *Int. J. Heat Mass Transfer* **2005**, *48*, 2150−2158.
(26) Notario, B.; Pinto, J.; Solorzano, E.; De Saja, J. A.; Dumon, M. Experimental validation of the Knudsen effect in nanocellular polymeric foams. *Polymer* **2015**, *56*, 57−67.
(27) Lu, X.; Caps, R.; Fricke, J.; Alviso, C. T.; Pekala, R. W. Correlation between structure and thermal conductivity of organic aerogels. *J. Non. Cryst. Solids.* **1995**, *188*, 226−234.
(28) Manawi, Y. M.; Khraisheh, M. A. M. M.; Kayvani, A.; Benyahia, F.; Adham, S. A predictive model for the assessment of the temperature polarization effect in direct contact membrane distillation desalination of high salinity feed. *Desalination* **2014**, *341*, 38−49.
(29) Boudenne, A.; Ibos, L.; Gehin, E.; Candau, Y. A simultaneous characterization of thermal conductivity and diffusivity of polymer materials by a periodic method. *J. Phys. D. Appl. Phys.* **2004**, *37*, 132.
(30) Price, D. M.; Jarratt, M. Thermal conductivity of PTFE and PTFE composites. *Thermochim. Acta* **2002**, *393*, 231−236.
(31) Chen, L.; Xu, H.-F.; He, S.-J.; Du, Y.-H.; Yu, N.-J.; Du, X.-Z.; Lin, J.; Nazarenko, S. Thermal Conductivity Performance of Polypropylene Composites Filled with Polydopamine-Functionalized Hexagonal Boron Nitride. *PLoS One* **2017**, *12*, e0170523.
(32) Weidenfeller, B.; Höfer, M.; Schilling, F. R. Thermal conductivity, thermal diffusivity, and specific heat capacity of particle filled polypropylene. *Compos. Part A* **2004**, *35*, 423−429.
(33) Bonno, B.; Laporte, J. L.; Tascón d'León, R. Determination of thermal parameters of PVDF using a photoacoustic technique. *Meas. Sci. Technol.* **2001**, *12*, 671−675.
(34) dos Santos, W.N.; Iguchi, C.Y.; Gregorio, R. Thermal properties of poly(vinilidene fluoride) in the temperature range from 25 to 210° C. *Polym. Test.* **2008**, *27*, 204−208.

https://doi.org/10.1021/acsestengg.2c00436
ACS EST Engg. 2023, 3, 874−882